View metadata, citation and similar papers at core.ac.uk

brought to you by CORE

provided by Open Archive Toulouse Archive Ouverte

Open Archive Toulouse Archive Ouverte

OATAO is an open access repository that collects the work of Toulouse researchers and makes it freely available over the web where possible

This is an author's version published in: https://oatao.univ-toulouse.fr/26834

Official URL :
https://doi.org/10.1016/j.materresbull.2020.110940

To cite this version:

Duployer, Benjamin and Tenailleau, Christophe and Thimont, Yohann and Lenormand, Pascal and Barnabé, Antoine and Presmanes, Lionel *Preparation and study of CuBi2O4 thin films by RF magnetron sputtering*. (2020) Materials Research Bulletin, 130. ISSN 0025-5408

Any correspondence concerning this service should be sent
to the repository administrator: tech-oatao@listes-diff.inp-toulouse.fr

Preparation and study of $CuBi_2O_4$ thin films by RF magnetron sputtering

Benjamin Duployer, Christophe Tenailleau*, Yohann Thimont, Pascal Lenormand, Antoine Barnabé, Lionel Presmanes

CIRIMAT, Université de Toulouse, CNRS, Université Toulouse 3 - Paul Sabatier, 118 Route de Narbonne, 31062 Toulouse Cedex 9, France

A R T I C L E I N F O

Keywords:
Thin film
$CuBi_2O_4$
Bi_2CuO_4
Sputtering
Band gap
Raman spectroscopy
Optical constants n and k

A B S T R A C T

Copper bismuth oxide ($CuBi_2O_4$ or Bi_2CuO_4) thin films have been elaborated for the first time by radio-frequency magnetron sputtering using a homemade $CuBi_2O_4$ ceramic target. X-ray diffraction characterizations revealed an amourphous phase for as-deposited films. After air annealing at 450 °C for 12 h, a pure polycristalline $CuBi_2O_4$ phase can been obtained. Raman spectroscopy confirmed the film phase purity. The influence of the thickness on the structural properties of the films has been studied and we observed that all films treated above 450 °C are crystallized. The thinner films show preferred orientation while there are less crystal defects for the thickest films (~700 nm). Atomic force microscopy shows a homogeneous polycristalline microstructure at the surface of the film. Optical measurements performed by UV–vis-IR spectrophotometry indicate that these films have one of their optical band gaps in the visible region (E_g~1.5 eV) which makes them suitable as thin films solar absorption materials.

1. Introduction

The ternary compound $CuBi_2O_4$ possesses an unusual crystal structure with stacks of square planar CuO_4 groups linked to distorted trigonal BiO_6 polyhedra, associated with very interesting electrical and antiferromagnetic properties [1,2]. In recent years, this p-type semiconductor has been identified as a promising material for its use in photocatalystis, photoelectrochemistry and the generation of hydrogen from water [3–5]. Indeed, it was reported that $CuBi_2O_4$ has an optical absorption onset of 1.4–1.8 eV although it is not yet clear whether the band gap is direct or indirect [6]. Moreover, its conduction band minimum is located on a more negative position than the water reduction potential, enabling solar H_2 production [7–9].

Up to now, all $CuBi_2O_4$ thin films reported were synthesized by electrodeposition [10,11], hydrothermal synthesis [8], sol gel method [12], or spray pyrolysis [13], essentially. Among all deposition methods, sputtering deposition (Physical Vapor Deposition or PVD) is a simple, industrial and environmentally friendly technique that can provide dense and homogenous oxide thin films with a good control of their thicknesses and excellent adhesion. A post-thermal annealing has often to be carried out in order to get a fully crystalline material. In the case of stable oxides, this thermal annealing can be a simple and conventional annealing treatment performed in air, which is less expensive than thermal annealing under vacuum, neutral gas, or complex atmosphere. By easily controlling the sputtering parameters, playing on the pressure to vary the porosity for example [14], the properties of the films can be optimized for various applications.

However, to the best of our knowledge there is no publication yet about the use of the radio-frequency (RF) sputtering technique for its deposition.

In this work, we thus report for the first time the preparation of $CuBi_2O_4$ thin films by the PVD technique and their structural, microstructural and optical characterizations.

2. Experimental

2.1. Film preparation

Thin films were deposited by RF magnetron sputtering using a homemade $CuBi_2O_4$ ceramic target. Indeed, a stoichiometric mixture of CuO and Bi_2O_3 commercial powders was first heated at 770 °C (below the eutectic point) for 48 h in air to get a pure $CuBi_2O_4$ phase (checked by X-ray diffraction). The polycrystalline $CuBi_2O_4$ powder (150 g) was then pressed in a die of 10 cm in diameter and sintered at 770 °C for 12 h under air atmosphere. The relative density of the target was about 75 %. X-Ray Diffraction (XRD) measurements carried out on a small representative pellet showed no impurity phase.

The sputtering apparatus is an ALCATEL A450 with a radio-frequency generator (13.56 MHz) and a pumping system (limit pressure P = 5.10^{-5} Pa inside the deposition chamber before deposition). The RF

* Corresponding author.
E-mail address: tenailleau@chimie.ups-tlse.fr (C. Tenailleau).

Table 1
Deposition parameters.

Deposition parameters
Target Diameter (cm) 10
Target-to-substrate distance (cm) 5
RF power (W) 20
Magnetron yes
Sputtering gas Ar
Background pressure (Pa) 5.10^{-5}
Working pressure (Pa) 0.5
Argon flow rate (sccm) 11
Deposition rate (nm. min^{-1}) 6.25
Film thickness (nm) 100 – 300-700
Substrate holder water cooled

power was fixed at 20 W. Pre-sputtering by argon plasma was performed during 15 min to clean the target surface of any impurity prior to the film deposition. Pre-cleaned 1 mm thick microscopy slides, convenient due to their high transparency, intermediate thermal dilatation coefficient and low cost, were used as substrates.

The deposition parameters are summarized in Table 1. The analysis of the chemical composition of the films made by electron probe microanalysis (using a Cameca SX 50 apparatus) confirmed the conservation of the target composition into the film. The sample showed a Cu/Bi ratio close to 0.5 and a general formula of Cu1.02(4)Bi1.9(2)O4.10(4) was determined for all samples analyzed.

Thickness measurements were performed by surface profilometry, using a DEKTAK 3030ST mechanical profilometer, and by X-Ray Reflectivity (XRR), using a Bruker D8 Advance diffractometer equipped with a Göbel mirror. The experimental XRR data were fitted using a modified Fresnel recursive formula, generally referred as the Parratt formalism [15]. All measurements we made on as-deposited samples.

2.2. Characterizations

Structural characterizations of films were performed using a Bruker D8 diffractometer in the Bragg-Brentano configuration. Data were recorded using a CuK_{α} wavelength radiation (40 kV, 40 mA) and collected over the $10° < 2\Theta < 100°$ range at room temperature with a 0.02 step scan and 20 s/step. Nickel filter was used to eliminate the K_{β}-ray and reduce fluorescence.

Raman spectra were collected under ambient conditions using a LabRAM HR 800 Jobin Yvon spectrometer with a laser excitation wavelength of 532 nm. Spectra acquisitions were carried out for 300 s using x100 objective lens and 600 g/mm grating. Examination of multiple spots showed that the deposited sample were homogeneous.

To study the microstructure of the films, Atomic Force Microscopy (AFM) Veeco Dimension 3000 equipped with a super sharp TESP-SS Nanoworld tip was used. AFM surface images were analysed using the Gwyddion Software.

The electrical measurements were made with a QuadPro four-point probe device from Signatone equipped with a Keithley SMU 237. This type of system can measure a maximum resistance of 10^{10} Ω.

The optical characteristics of thin films were investigated in the 300–1100 nm wavelength range using a Bentham PVE300 integrated spectrophotometer. The optical transmittance of the glass substrate was systematically subtracted from the final data before calculation. Spectra were then modeled using the SCOUT software [16].

3. Results and discussion

3.1. Thickness determination

To calibrate the thicknesses of the layers, we used two different techniques. First, an uniform deposition rate equal to 6.25 $nm.min^{-1}$ in the 25–700 nm range has been determined by measuring walking heights with a mechanical profilometer. We then proceeded to XRR measurements for showing that our deposition technique can be used for the preparation of a dense, controlled in thickness and homogenous thin layer of $CuBi_2O_4$.

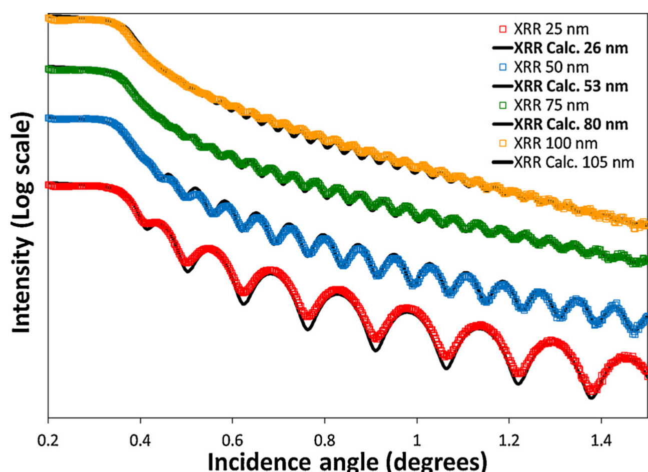

Fig. 1. X-Ray reflectivity curves for a $CuBi_2O_4$ thin film. Full line is the best fit calculated from the recursive Parratt formalism.

From the Parratt's formalism and in the case of one simple layer, the specular reflection coefficient R is expressed as:

$$R = \left| \frac{r_1 + r_2 e^{-2ik_2 d}}{1 + r_1 r_2 e^{-2ik_2 d}} \right|^2$$

Where r_1 an r_2 are the Fresnel reflection coefficient for respectively the air/layer (r_1) and the layer/substrate (r_2) interfaces, k_2 the wave vector's normal component of the electromagnetic wave propagating in the layer and d the thickness.

The Fresnel reflection coefficient depends upon the incident angle in between the beam and the sample surface as well as the refractive index of the considered material. When the chemical composition is well-known, the refractive index is expressed depending on the density. So the fit of the experimental data has been done by considering both thickness and density as adjustable parameters.

Fig. 1 shows the X-Ray Reflectivity curves for samples with theoretical thicknesses of 25 nm, 50 nm, 75 nm and 100 nm. These curves exhibit well marked oscillations, known as Kiessig fringes [17], which are characteristics of continuous, homogenous and uniform layers with low surface and interface roughness. Full lines correspond to the best fitting curves from which the thickness and the density are deduced. The values obtained (26 nm, 53 nm, 80 nm and 105 nm for thicknesses; 8.4 $g.cm^{-3}$ for density) are very close to the theoretical ones. This confirms that it is possible to produce thin films with a precise and homogeneous thickness and a high density using the sputtering technique, which is an important advantage over other deposition techniques.

3.2. Structural and microstructural characterizations

Thicker samples have been studied in order to have a better diffraction signal and to better characterize the purity of the thin film.

The substrates used in this work were microscopy slices, made out of 1 mm thick soda-lime glass (~ 5 cm^2 square substrates). Although the softness temperature is usually around 750 °C, according to some supplier references, it can be around 550 °C, close to the treatment temperature chosen in this paper. In addition, this choice was also justified by the fact that most of the n-type TCOs on which our material could be superimposed for future electronic and energy applications are stable in this temperature range.

A first sample of 700 nm has been first deposited and studied. Fig. 2

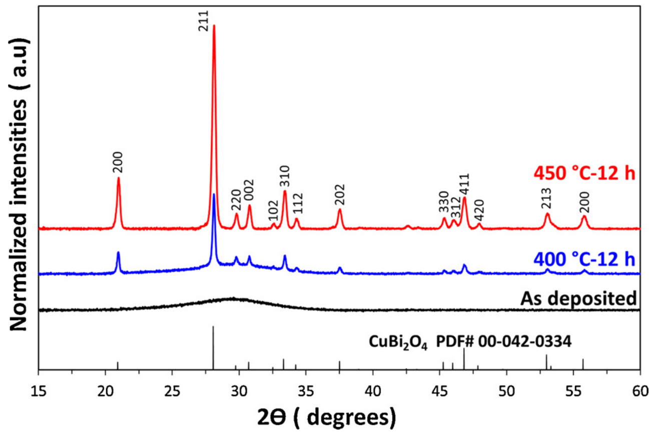

Fig. 2. X-Ray diffraction patterns of thin films as deposited and annealed at different temperatures.

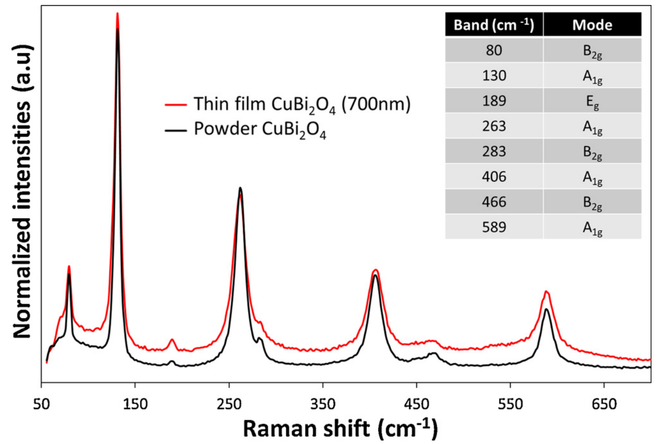

Band (cm⁻¹)	Mode
80	B_{2g}
130	A_{1g}
189	E_g
263	A_{1g}
283	B_{2g}
406	A_{1g}
466	B_{2g}
589	A_{1g}

Fig. 3. Raman spectra of $CuBi_2O_4$ powder and thin film (700 nm after annealing at 450 °C).

shows the XRD patterns of $CuBi_2O_4$ thin films studied (as-deposited and annealed under air at 400 °C and 450 °C for 12 h). The as-deposited sample shows no diffraction peak which indicates an amorphous or nanocrystallized sample.

From 400 °C, the film begins to crystallize. Peaks of low intensity correspond to the crystalline structure of $CuBi_2O_4$, whereas the broad hump in the background shows that there is still some amorphous phase that remains, thus evidencing that this temperature is not sufficient to have a good crystallization for this lap of time.

It is from twelve hours of annealing at 450 °C in air (suitable temperature for a glass substrate) that the sample has the best crystallized state and the XRD diffraction pattern corresponds to the reference pattern # 00-042-0334 of the ICDD Powder Diffraction File (PDF®)database. This result shows that the film consists of a pure polycrystalline $CuBi_2O_4$ with a tetragonal crystal structure (*P4/nnc* space group). Our cell parameters determined at room temperature by profile matching using the Fullprof Sofware are $a = 8.4945(7)$ Å and $c = 5.8199(5)$ Å [18]. An apparent crystallite size of 70 nm has been estimated from the total Full Width at Half Maximum (FWHM) considering only the main (211) Bragg peak corrected from the instrumental contribution (*i.e.* assuming that the microstrain are negligible), applying a pseudo-distribution for the peak broadening, and using Scherrer's formula:

$$D = \frac{0.9\lambda}{FWHM^{sample}\cos\theta}$$

where D is the crystallite size, $FWHM^{sample}$ is the full width at half-maximum corrected from experimental broadening, λ is the X-ray wavelength (1.54056 Å) and θ is the Bragg angle.

This 700 nm thin film annealed at 450 °C has been also investigated by Raman spectroscopy. A comparison with our reference powder used for the target was made and the spectra are depicted in Fig. 3. The sputter-deposited film shows exactly the same spectrum than the $CuBi_2O_4$ target. This demonstrates that the sputtering technique did not modify the stoichiometry of the compound. These results are also in agreement with the literature. Indeed our samples show the same features than for a bulk sample of $CuBi_2O_4$ synthesized by the traditional solid-state reaction method in air and reported by Popovic et al. [19]. Eight Raman bands are observed and centered at 80, 130, 189, 263, 283, 406, 466 and 589 cm^{-1}. The band at 80 cm^{-1} corresponds to the B_{2g} mode and is attribued to in-plane bond bending vibration of the rhombohedra. The strong peak at 130 cm^{-1} represents the A_{1g} mode which originates from translational vibrations of the CuO_4 planes along the z axis. The small peak at 189 cm^{-1} is the E_g mode and indicates the vibration of Cu-Cu links. The A_{1g} mode at 263 cm^{-1} corresponds to the rotation of two staked CuO_4 squares in opposite directions. The peaks at 280 cm^{-1} and 466 cm^{-1}, corresponding to B_{2g} modes, are assigned mainly from the oxygen motion. The band observed at 406 cm^{-1} is the A_{1g} mode of the Bi-O stretching vibration while the peak at 589 cm^{-1} is an in-plane breathing of CuO_4 squares.

These two complementary structural characterization techniques (XRD and Raman) show that it is possible to produce 700 nm films of $CuBi_2O_4$ using the sputtering technique. With a simple annealing stage at 450 °C in air, we can obtain well crystallized films with very high purity.

After optimization of the crystallization temperature, the influence of the thickness on the structural properties of the films was studied. XRD patterns of the $CuBi_2O_4$ films with 3 different film thicknesses are shown in Fig. 4.

All films are polycrystalline, and the major peaks corresponding to the tetragonal $CuBi_2O_4$ (PDF®. # 00-042-0334) are observed. The cell parameters a and c, determined at room temperature by profile matching, are reported in Table 2. The values are in good agreement with the reference PDF® pattern and no signifiant effect of the thickness on the cell parameters is observed.

In order to have information about the level of crystallinity in these films, one can look at the evolution of the crystallite size (D) and the dislocation density (δ) according to the thickness.

The dislocation density, defined as the length of dislocation lines per unit volume of the crystal, was evaluated from the formula [20] :

$$\delta = \frac{1}{D^2}$$

All of these values, calculated for the most intense (211) diffraction peak, are given in Table 2.

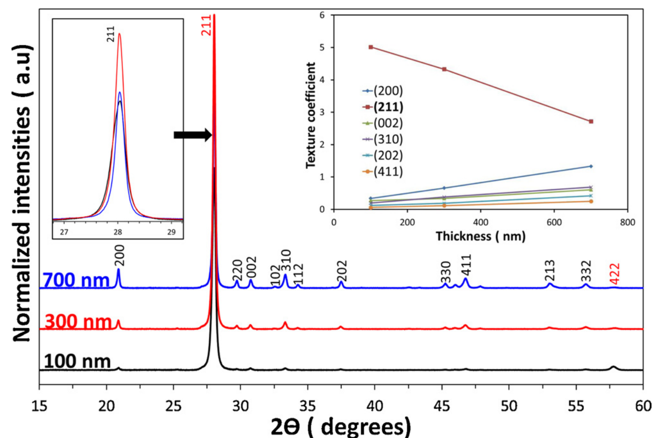

Fig. 4. X-Ray diffraction patterns of $CuBi_2O_4$ thin films for various thicknesses. Insert shows the variation of the texture coefficient for different (hkl) planes.

Table 2
Structural parameters of $CuBi_2O_4$ thin films at different thicknesses from (211) peaks.

Thickness (nm)	FWHM (degrees)	Crystallite size D (nm)	Dislocation density δ (nm^{-2})	Cell parameters a (Å) c (Å)
100	0.278	35	8×10^{-4}	8.5129(5) 5.8155(8)
300	0.177	60	3×10^{-4}	8.4989(6) 5.8127(6)
700	0.166	70	2×10^{-4}	8.4945(7) 5.8199(5)

The crystallite size of the films increased from 35 to 70 nm with increasing thickness. The low dislocation density value for a thickness of 700 nm confirms the good level of crystallization, with less crystal defects in each film.

Fig. 4 also shows a significant effect of the film thickness on the diffraction peak intensity ratios. Indeed, all the peak intensities increase proportionally with the thickness except for the (211) and (422) orientations. Harris' relation can be used to understand the quantitative relation between the peak intensity and orientation [21]:

$$TC(hkl) = \frac{\frac{I(hkl)}{I_0(hkl)}}{N^{-1}\sum\frac{I(hkl)}{I_0(hkl)}}$$

where TC(hkl), known as the texture coefficient, qualitatively defines the preferential orientation of the thin film. I(hkl) is the intensity of a particular plane from the recorded XRD pattern and I_0(hkl) is the intensity of the corresponding plane from a standard ICDD pattern. N is the number of diffraction peaks used in the calculation.

Insert in Fig. 4 shows the variation of the texture coefficient for different (hkl) planes. We can observe a strong preferred orientation for the (211) plane that decreases when the thickness increases from 100 nm to 700 nm. In other words, if the film grains are preferentially oriented, an anisotropy of the material properties could then be observed.

AFM images of $CuBi_2O_4$ thin films have been taken in order to complete the microstructural information and confirm these results (Fig. 5). A 700 nm as-deposited sample and three others of 100 nm, 300 nm and 700 nm annealed at 450 °C are here compared.

From these images, we can first see the significant effect of annealing on the microstructure of the samples. Indeed, for the 700 nm sample, the surface grain diameter increased after annealing at 450 °C, in comparaison to the as-deposited sample. The in-plane average grain size was estimed by an immersion threshold method thanks to the Gwyddion software [22]. The mean diameter increased from 20 nm for the as-deposited sample to 60 nm for the annealed sample. This grain size is close to the value of the crystallite size determined by XRD.

It is also noted that the thickness influences the homogeneity and the density of the film. In fact, the thinnest films seem to be composed of aggregates with a fairly large dispersion. The roughness decreases with thickness. With a R_a value of 9 nm for the 100 nm film to 5 nm for the thickest film (700 nm). The images also seem to show much more grain boundaries and pinholes for the 100 nm and 300 nm samples than for the 700 nm film. These observations are in agreement with the values of dislocation density calculated previously.

3.3. Electrical and optical properties measurements

3.3.1. Electrical resistivity

The plots of the I–V characteristics are shown in Fig. 6. Measurements have been made at room temperature, 100 °C and 150 °C for films of different thicknesses. However, it can be noted that for the 100 nm film the measurements are only possible from 150 °C and for that of 300 nm from 100 °C. The resistance values are otherwise too high for the system. The linear nature of the I–V charateristics confirms an

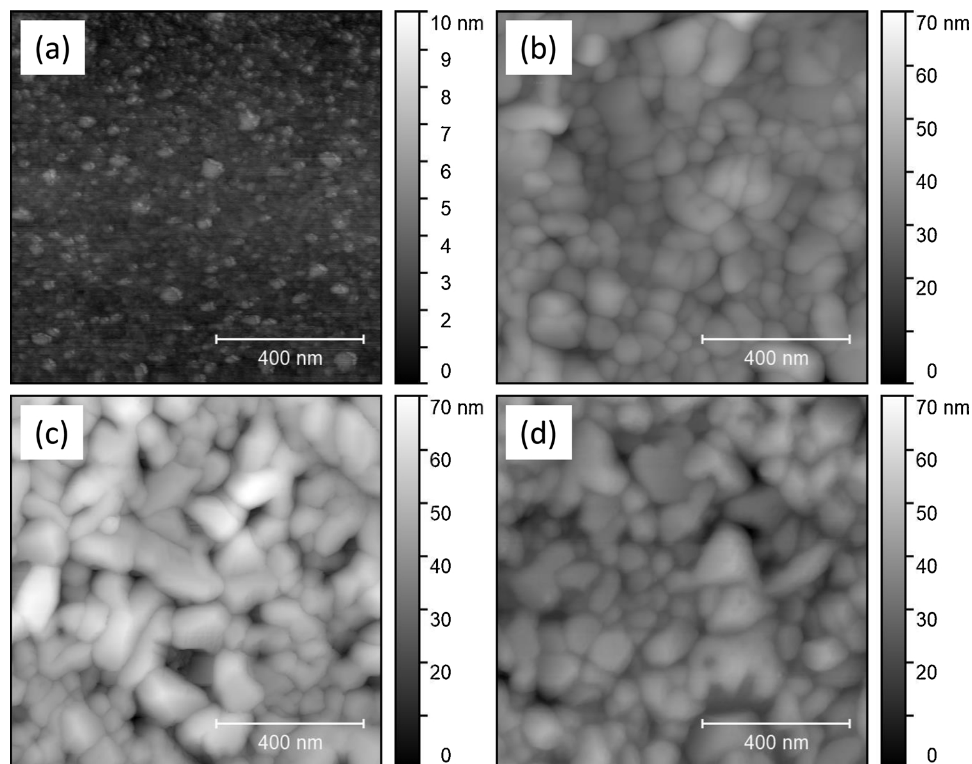

Fig. 5. AFM images of $CuBi_2O_4$ thin films: (a) 700 nm as deposited, (b) 700 nm (c) 100 nm (d) 300 nm after annealing at 450 °C.

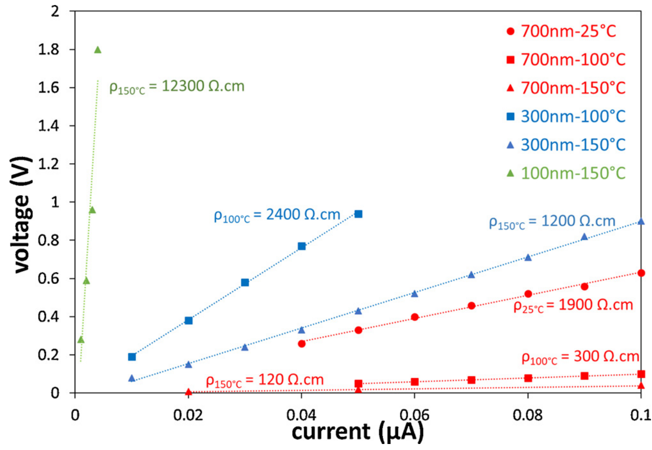

Fig. 6. Current–voltage (I–V) curves for $CuBi_2O_4$ films.

ohmic character of all $CuBi_2O_4$ films. From these measurements, a resistivity value can be calculated for each thickness and each temperature (given in Fig. 6). The observed behavior of the electrical resistivity, with respect to the variation in resistivity, is representive of a conventional semiconductor material. Indeed, the resistivity decreases with the increasing temperature. Note that the resistivity is lower for the thickest films, which is probably due to the presence of lower grain boundaries concentration. From this data and for the 700 nm film, an activation energy (E_a = 0.24 eV) was obtained, which corresponds to the separation between the Fermi level and the valence band.

3.3.2. Optical properties

Fig. 7a and b show the integrated Total Transmittance (TT) and Total Reflectance (TR) optical spectra variations of a 700 nm thick film annealed at 450 °C and the corresponding simulated TT and TR spectra.

TT and TR spectra were fitted simultaneously thanks to dielectric models, which integrate a Kramer Kronig relationship for interband transition [23] and Kim oscillators [24]. A good match between experimental and simulated TT and TR spectra has been found (standard deviation of 1.6×10^{-4} and 5.8×10^{-5} for TT and TR, respectively) and the model allowed to obtain a good estimation of the film thickness of 685 nm, in agreement with the measurements done by profilometry (690 nm).

The variations of the optical index n and k in the 300 − 1000 nm range, which have been deduced from this model, are presented in Fig. 7c.The values are similar to those obtained by Manley et al. [25] with a spectroscopy ellipsometer on a single crystal of $CuBi_2O_4$.

Using the absorption coefficient deduced from the optical simulation, we generated the Tauc plots over the same spectral range (shown in Fig. 8) and determined both direct and indirect bandgap by linear extrapolations to the energy axis.

A direct band gap E_{gd} close to 3.5 eV can be determined. It would correspond to the transition between the O_{2p} and Cu_{3d} orbitals. However, two indirect band gap can also be determined at lower energies with an exponent of 1/2 for the $(\alpha.h.\nu)$ *vs* E by drawing the Tauc plots. The highest band at $E_{gi,1}$ = 2.6 eV would also correspond to a O_{2p} and Cu_{3d} transition, while the value of the lowest band energy transition $E_{gi,2}$ = 1.5 eV would be associated to Bi_{6s} and Cu_{3d} transitions. The lowest energy values determined here are in agreement with the p-DOS diagram found in the litterature and calculated by Sharma et al. [8].

This lower bandgap value in the visible range makes those $CuBi_2O_4$ thin films deposited by RF sputtering also very interesting for solar energy applications.

4. Conclusion

$CuBi_2O_4$ thin films were deposited for the first time by RF

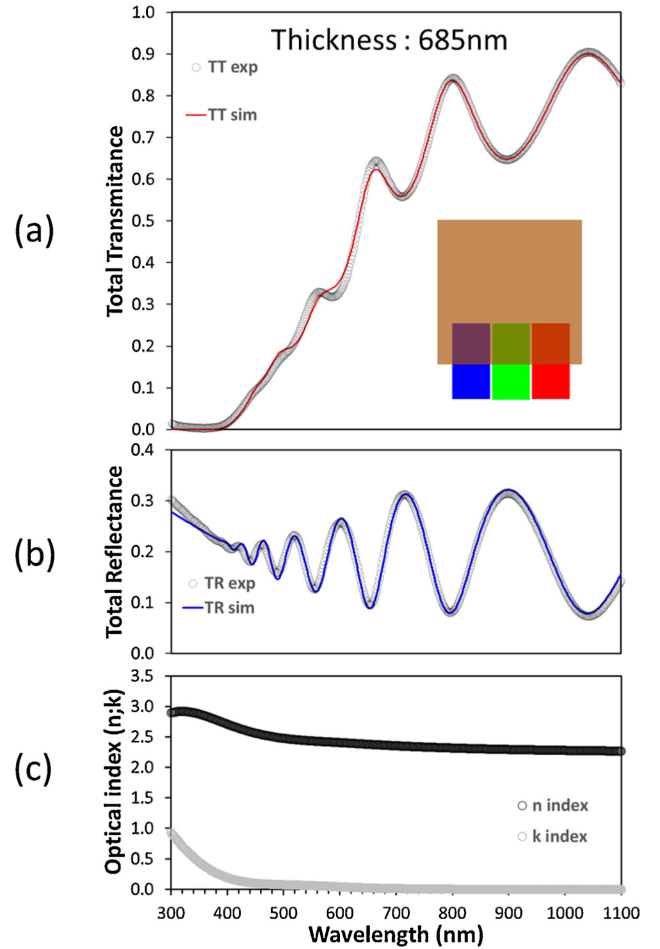

Fig. 7. (a) TT (b) TR optical spectra of 700 nm thin films annealed at 450 °C. (c) Optical index n and k plotted as a function of wavelength for the $CuBi_2O_4$ thin film.

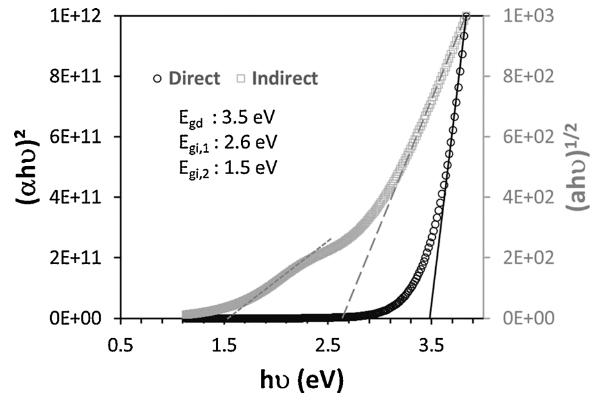

Fig. 8. Plots of $(\alpha h\nu)^2$ and $(\alpha h\nu)^{1/2}$ as a function of photon energy for the $CuBi_2O_4$ thin films.

magnetron sputtering and characterized by XRD, Raman, AFM, and UV–vis-IR spectrophotometry measurements. These films, after heat treatment at 450 °C in air, show a pure $CuBi_2O_4$ phase with good cristallinity. The microstructure is homogeneous and dense with a nanometric grain size. Two indirect optical band gaps were measured at 2.6 and 1.5 eV in accordance with the bulk material. Due to the fact that the post-deposition annealing stage can be carried out at moderate temperature, the RF magnetron sputtering technique can provide an easy access route to cristalline thin films of $CuBi_2O_4$ on glass substrate.

Authorship contributions

Category 1

Conception and design of study: Christophe Tenailleau, Lionel Presmanes, Benjamin Duployer;

acquisition of data: Benjamin Duployer, Antoine Barnabé, Yohann Thimont, Pascal Lenormand;

analysis and/or interpretation of data: Benjamin Duployer, Antoine Barnabé, Yohann Thimont, Pascal Lenormand, Christophe Tenailleau, Lionel Presmanes;

Category 2

Drafting the manuscript: Benjamin Duployer, Christophe Tenailleau, Lionel Presmanes;

revising the manuscript critically for important intellectual content: Benjamin Duployer, Antoine Barnabé, Yohann Thimont, Pascal Lenormand, Christophe Tenailleau, Lionel Presmanes;

Category 3

Approval of the version of the manuscript to be published:

Benjamin Duployer, Antoine Barnabé, Yohann Thimont, Pascal Lenormand, Christophe Tenailleau, Lionel Presmanes.

Declaration of Competing Interest

The authors declare that they have no known competing financial interests or personal relationships that could have appeared to influence the work reported in this paper.

Acknowledgements

The French FERMAT Federation FR3089 is acknowledged for financial support to the D8 XRD instrument.

Appendix A. Supplementary data

Supplementary material related to this article can be found, in the online version, at doi:https://doi.org/10.1016/j.materresbull.2020.110940.

References

[1] J.L. Garcia-Munoz, J. Rodriguez-Carjaval, F. Sapina, M.J. Sanchis, R. Ibanez, D. Beltran-Porter, Crystal and magnetic structures of Bi2CuO$_4$, J. Phys. Condens. Matter 2 (1990) 2205–2214.

[2] J. Konstantinovic, G. Stanisic, M. Ain, G. Parette, On the magnetic structure of Bi_2CuO_4, J. Phys. Condens. Matter 3 (1991) 381–384.

[3] T. Arai, Y. Konishi, Y. Iwasaki, H. Sugihara, K. Sayama, High-throughput screening using porous photoelectrode for the development of visible-light-responsive semiconductors, J. Comb. Chem. 9 (2007) 574–581.

[4] A. Elaziouti, N. Laouedj, A. Bekka, Synthesis, characterization and UV-A light photocatalytic activity of 20 wt%SrO–$CuBi_2O_4$ composite, Appl. Sur. Sci 258 (2012) 5010–5024.

[5] H. Gao, F. Wang, S. Wang, X. Wang, Z. Yi, H. Yang, Photocatalytic activity tuning in a novel Ag2S/CQDs/CuBi2O4 composite: synthesis and photocatalytic mechanism, Mater. Res. Bull. 115 (2019) 140–149.

[6] D. Roy, G. Samu, M. Hossain, C. Janaky, K. Rajeshwar, On the measured optical bandgap values of inorganic oxide semiconductors for solar fuels generation, Catal. Today 300 (2018) 136–144.

[7] R. Patil, S. Kelkar, R. Naphade, S. Ogale, Low Temperature Grown CuBi2O$_4$ with flower Morphology and its composite with CuO nanosheets for photoelectrochemical water splitting, J.Mater. Chem A 2 (2014) 3661–3668.

[8] G. Sharma, Z. Zhao, P. Sarker, B.A. Nail, J. Wang, M.N. Huda, F.E. Osterloh, Electronic structure, photovoltage, and photo-catalytic hydrogen evolution with p-$CuBi_2O_4$ nanocrystals, J. Mater. Chem. A Mater. Energy Sustain. 4 (2016) 2936–2942.

[9] H.S. Park, C.Y. Lee, E. Reisner, Photoelectrochemical reduction of aqueous protons with a CuO / $CuBi_2O_4$ Heterojunction under visisble light irradation, Phys. Chem. Chem. Phys. 16 (2014) 22462–22465.

[10] D. Cao, N. Nasori, Z. Wang, Y. Mi, L. Wen, Y. Yang, S. Qu, Z. Wang, Y. Lei, p-Type $CuBi_2O_4$: an easily accessible photocathodic material for high-efficiency water splitting, J. Mater. Chem A 4 (2016) 8995–9001.

[11] D. Kang, J.C. Hill, Y. Park, K.-S. Choi, Photoelectrochemical properties and photostabilities of high surface area $CuBi_2O_4$ and Ag-doped $CuBi_2O_4$ photocathodes, Chem. Mater. 28 (2016) 4331–4340.

[12] J. Zhang, Y. Jiang, Preparation, characterization and visible photocatalytic activity of $CuBi_2O_4$ phtocatalyst by a novel sol-gel method, J. Mater. Sci 26 (2015) 4308–4312.

[13] F. Wang, A. Chemseddine, F.F. Abdi, R. Van de Krol, S.P. Berglund, Spray pyrolysis of $CuBi_2O_4$ photocathodes: improved solution chemistry for highly homogeneous thin films, J. Mater. Chem. 5 (2017) 12838–12847.

[14] F. Oudrhiri-Hassani, L. Presmanes, A. Barnabé, P.T. ailhades, Microstructure, porosity and roughness of RF sputtered oxide thin films:characterization and modelization, Appl. Sur. Sci. 254 (2008) 5796–5802.

[15] L.G. Parrat, Surface studies of solids by total reflection of X-Rays, Phys. Rev. 95 (1954) 359.

[16] W. Theiss; Hard & Software. http://www.mtheiss.com/.

[17] H. Kiessig, Ann.Phys. 10 (1931) 769.

[18] J. Rodríguez-Carvajal, FullProf: a program for rietveld refinement and profile matching analysis of complex powder diffraction patterns, Physica B. 192 (1993) 55.

[19] Z.V. Popovic, G. Kliche, M. Cardona, R. Liu, Vibrational properties of Bi_2CuO_4, Phys. Rev. B 41 (1990) 3824–3828.

[20] G.B. Williamson, R.C. Smallman, Dislocation densities in some annealed and cold-worked metals from measurements on the X-ray debye-scherrer spectrum, Philos. Mag. 1 (1956) 34.

[21] C. Barrett, T.B. Massalki, Structure of Metals, Pergamon, Oxford, 1980, p. 204.

[22] D. Necas and P. Klapetek, http://www.gwyddion.net/ Gwyddion software.

[23] F. Demichelis, G. Kaniadakis, A. Tagliaferr, E. Tresso, New approach to optical analysis of absorbing thin solid films, Appl. Opt. 26 (1987) 1737.

[24] C.C. Kim, J.W. Garland, H. Abad, P.M. Raccah, Modeling the optical dielectric function of semiconductors : extension of the critical-point parabolic-band approximation, Phys. Rev. B : Condens. Matter Mater. Phys. 45 (1992) 11749.

[25] P. Manley, F.F. Abdi, S. Berglund, A.T.M.N. Islam, S. Burger, R. Van de Krol, M. Schmid, Absorption enhancement for ultra-thin solar fuel devices with plasmonic gratings, App. Ener. Mat. 1 (2018) 5810–5815.